ACS APPLIED MATERIALS & INTERFACES

Research Article

www.acsami.org

Nanosheet-Structured Boron Nitride Spheres with a Versatile Adsorption Capacity for Water Cleaning

Fei Liu, Jie Yu,* Xixi Ji, and Muqi Qian

Shenzhen Engineering Lab of Flexible Transparent Conductive Films, Shenzhen Key Laboratory for Advanced Materials, and Department of Material Science and Engineering, Shenzhen Graduate School, Harbin Institute of Technology, University Town, Shenzhen 518055, China

ABSTRACT: Here, we report the synthesis of nanosheet-structured boron nitride spheres (NSBNSs) by a catalyzing thermal evaporation method from solid B powders. The NSBNSs consist of radially oriented ultrathin nanosheets with the sheet edges oriented on the surface. Formation of this unique structure occurs only at a certain reaction temperature. The diameter from 4 μm to 700 nm and the nanosheet thickness from 9.1 to 3.1 nm of the NSBNSs can be well-controlled by appropriately changing the mass ratio of boron powders and catalyst. The NSBNSs possess versatile adsorption capacity, exhibiting excellent adsorption performance for oil, dyes, and heavy metal ions from water. The oil uptake reaches 7.8 times its own weight. The adsorption capacities for malachite green and methylene blue are 324 and 233 mg/g, while those for Cu^{2+}, Pb^{2+}, and Cd^{2+} are 678.7, 536.7, and 107.0 mg/g, respectively. The adsorption capacities of the NSBNSs for Cu^{2+} and Pb^{2+} are higher or much higher than those of the adsorbents reported previously. These results demonstrate the great potential of NSBNSs for water treatment and cleaning.

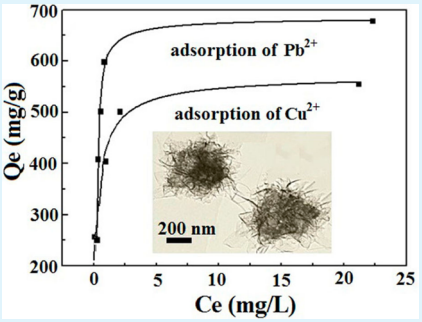

KEYWORDS: *boron nitride, nanosheets, spheres, adsorption, water cleaning*

1. INTRODUCTION

Two-dimensional (2D) nanosheets with nanoscale thickness have attracted great interest due to the high specific surface area (SSA) and abundant edge sites with high activity.[1,2] The nanosheets possess many interesting properties arising from their unique structure, resulting in important applications in different areas such as catalysis,[3] sensors,[4] supercapacitors,[5,6] field emission,[7] and lithium-ion batteries.[8] However, the nanosheets suffer from the problem of aggregation during application, which reduces the effective surface area and active edge sites. As a result, the observed performance of nanosheets is generally poorer than that exhibited by the single ones. Therefore, it is important to take appropriate measures to solve the problem of aggregation and thus maximize the performance of the nanosheets. Up to now, different measures such as separating the nanosheets with nanoparticles[9] and immobilizing the nanosheets by growing on appropriate substrates[10] or assembling into three-dimensional (3D) architectures[11] have been reported, which show obvious beneficial effects. The 3D architectures such as graphene aerogel[12,13] could prevent aggregation of the constituent nanosheets and thus exhibit enhanced performance for applications such as supercapacitors and catalysis. With this consideration, a spherical structure with the nanosheets radially oriented is an appropriate architecture for full exposure of the surface and edge sites of the nanosheets.

Boron nitride (BN) with a structure similar to graphite possesses many extraordinary properties such as wide band gap, high oxidization resistance at high temperature, and high chemical stability.[14−17] These properties are complementary to graphite. In addition, similar to graphite, BN has a high thermal conductivity.[14] Because of these properties, BN is of high potential for various applications such as high frequency electronic devices,[18] ultraviolet light emission devices,[19] heat resisting materials,[20] composite materials,[21] superhydrophobic surfaces,[22] catalyst support,[23] and hydrogen storage.[24] A variety of BN nanostructures have been prepared, where the representative ones include nanotubes,[25] nanosheets,[22] nanobelts,[26] and nanofibers.[27] Among the different BN nanostructures, 2D nanosheets have been recently attracting more and more interest after the intensive research on the nanotubes. However, the preparation or assembly of the BN nanosheets into 3D architectures like spheres has been rarely reported comparing with other materials such as carbon, TiO_2, and SnO_2.[28−30] Therefore, it is interesting to find routes for preparing the spherical structure of BN nanosheets.

At present, environmental pollution is one of the most serious problems people are facing. Therefore, it is an urgent task to develop effective methods for eliminating the pollutants from water and air. Recently, it has been reported that nanostructural boron nitride has outstanding capability in absorbing organic pollutants and heavy metal ions from water, indicating high promise in environmental treatment. For instance, Zhang et al.[31] have synthesized BN nanocarpets composed of nanosheets and nanorods by a modified hot-press

Received: October 28, 2014
Accepted: December 31, 2014
Published: December 31, 2014

DOI: 10.1021/am507491z
ACS Appl. Mater. Interfaces 2015, 7, 1824−1832

benzenethermal method, which exhibit a high adsorption capacity of 272.4 mg/g for methylene blue (MB). Lei et al.[32] reported the synthesis of porous BN nanosheets with high SSA (1427 m^2/g), which can effectively absorb organic pollutants in water with the highest oil adsorption capacity reaching 3300%. Li et al.[33] synthesized activated boron nitride with very high SSA (2078 m^2/g) by a structure-directed thermal reaction method, which possesses excellent adsorption performance to various metal ions and organic pollutants with the adsorption capacity for Cr^{3+} reaching 352 mg/g. It is considered that the excellent and versatile absorption performance of the BN nanomaterials is mainly caused by the polarity of the B−N bond, large SSA, and swelling ability to accommodate intercalation.[31−33] However, to the best of our knowledge, the application of nanosheet-based BN spheres for pollutant removal has not been reported.

In this article, we report a simple catalyzing thermal evaporation approach to prepare the nanosheet-structured BN spheres (NSBNSs) with high controllability and high yield. The NSBNSs are composed of radially oriented ultrathin nanosheets with the sheet edges oriented on the surface. The NSBNSs possess excellent performance for application as adsorbents removing oil, dyes, and heavy metal ions from water. In particular, the adsorption capacities of the NSBNSs for Pb^{2+} and Cu^{2+} are higher or much higher than those of the adsorbents reported previously. The excellent adsorption performance of the NSBNSs mainly originates from the high-density edge sites on the surface.

2. EXPERIMENTAL SECTION

2.1. Preparation of Samples. The NSBNSs was prepared by a catalyzing thermal evaporation method from solid B powders. The catalyst was prepared by a sol−gel technique, which mainly consists of $CoFe_2O_4$ and CoO.

Catalyst Preparation. The starting solution was prepared by dissolving 0.33 g of $Fe(NO_3)_3{\cdot}9H_2O$ and 0.41 g of $Co(NO_3)_2{\cdot}6H_2O$ in 10 mL of distilled water to form a clear solution. After that, 3.3 g of citric acid was added to the solution, followed by heating at 90 °C for 4 h under magnetic stirring, obtaining a red sol. Citric acid functions as a complexing agent for metal ions and for controlling phase segregation during drying and initial thermal treatment of the gel.[34] Then, the sol was heated at 100 °C until a dried xerogel was formed. Lastly, the xerogel was heated at 600 °C in air for 10 min and then grinded into powders.

Growth of NSBNSs. In a typical procedure, B powders and the above prepared catalyst were first mechanically mixed. The mass ratios ($R_{B/C}$) of B powders and catalyst are 1:0.5, 1:1, 1:2, and 1:4, respectively. In each growth experiment, 400 mg of the mixture was put into the bottom of a crucible, which was then placed at the center of a tube furnace. Afterward, the mixture was heated at 1300 °C for 1 h in NH_3 with a flow rate of 120 sccm. During the temperature increasing process, N_2 was introduced at a flow rate of 100 sccm and then NH_3 was introduced after reaching 1300 °C. After growth reaction of 1 h, a large amount of white product can be obtained on the crucible walls (Figure 1).

2.2. Characterization Methods. The structure of the obtained samples was characterized by scanning electron microscopy (SEM, HITACHI S-4700), transmission electron microscopy (TEM, JEM-2100), Fourier transform infrared (FTIR, NICOLET-380) spectroscopy, Raman spectroscopy (Raman, Renishaw RM-1000), X-ray diffraction (Rigaku D/Max 2500Pc), and UV−visible absorption spectroscopy (Shimazu UV-2600 spectrophotometer). The specific surface area (SSA) of the samples was determined by nitrogen adsorption at 77 K (Belsorp II analyzer). The SSA was calculated using the Brunauer−Emmett−Teller (BET) method.

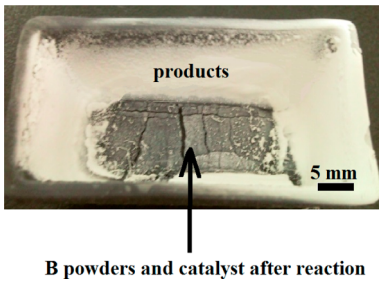

Figure 1. A photograph of the products deposited on the side wall of the crucible.

2.3. Adsorption Experiments. *Adsorption of Oil.* The pump oil was used as the target pollutant for testing the oil absorption capacity. A certain amount of pump oil was mixed with water to form an oil/water mixture. Then, a certain amount of the NSBNSs was dispersed in the oil/water mixture to absorb the oil. After full absorption, the NSBNSs with the absorbed oil were taken out for measurements. The oil absorption capacity (C_o) was calculated based on eq 1.

$$C_o = (W - W_0)/(W_0)\ (g/g) \quad (1)$$

In the equation, W is the total weight of the NSBNSs and the absorbed oil and W_0 is the weight of the pure NSBNSs.

Adsorption of Dyes. Malachite green (MG) and methylene blue (MB), acting as the target pollutants, were dissolved into deionized water to prepare the dye solutions with different concentrations. In a typical process, 10 mg of the NSBNSs was added into 25 mL of MG and MB solutions with a concentration of 110 mg/L under stirring for adsorption. After adsorption for the appropriate time, the NSBNSs were separated out from the solution by centrifugation. The concentration of the residue dyes in the solution was examined by UV−visible absorption.

Adsorption of Heavy Metal Ions. Heavy metal salt solutions with different concentrations were prepared by dissolving the appropriate amount of $CuSO_4{\cdot}5H_2O$, $Pb(NO_3)_2$, and $Cd(NO_3)_2$ in deionized water. During adsorption experiments, 10 mg of the NSBNSs was added into 25 mL of the above solution under magnetic stirring. After adsorption for the appropriate time, the NSBNSs were separated out by centrifugation and filtering. The initial concentration of heavy metal ion solution is 200 mg/L. The concentrations of heavy mental ions were determined by inductively coupled plasma-optical emission (ICP-MS, ELAN DRC-2).

To obtain the isotherms, the adsorption tests were performed for a series of solutions with different initial concentrations. Equilibrium adsorption capacity (Q_e, mg/g) on the dyes and heavy metal ions was calculated using the following equation:

$$Q_e = (C_0 - C_e)V/m \quad (2)$$

In the equation, C_0 and C_e (mg/L) are the initial and equilibrium concentrations of the dyes and heavy metal ions, V (l) is the volume of the solutions, and m (g) is the mass of the NSBNSs.

3. RESULTS AND DISCUSSION

Figure 2 shows the SEM images of the samples prepared at $R_{B/C}$ = 1:1 and different temperatures. It is clearly indicated that the morphology of the products is strongly dependent on the growth temperature. At 1100 °C, the products are irregular particles (Figure 2a), whereas, at 1400 °C, the products are a mixture of nanofibers and nanoparticles (Figure 2f). At the intermediate temperatures of 1200 and 1300 °C, the products exhibit a spherical morphology (Figure 2b−e). However, the spheres obtained at 1200 °C are composed of the striplike nanoparticles, and only at 1300 °C, the spheres composed of radially oriented nanosheets can be obtained. This nanosheet-structured BN spheres are abbreviated as NSBNSs here.

DOI: 10.1021/am507491z
ACS Appl. Mater. Interfaces 2015, 7, 1824−1832

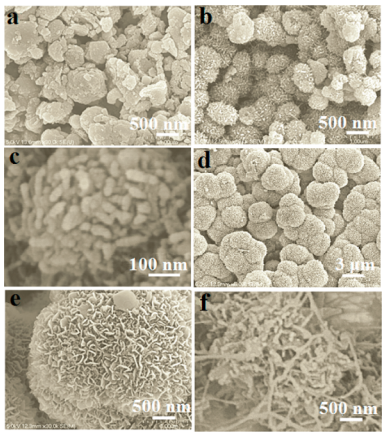

Figure 2. SEM images of the NSBNSs prepared at $R_{B/C}$ = 1:1 and different temperatures: (a) 1100 °C, (b, c) 1200 °C, (d, e) 1300 °C, (f) 1400 °C.

The effects of the catalyst amount used during the growth reaction on the structure of the NSBNSs were investigated at 1300 °C. Figure 3 shows the SEM images of the products prepared at 1300 °C and different $R_{B/C}$. It is found that the amount of the used catalyst plays important roles in the growth of the NSBNSs. With decreasing $R_{B/C}$ (increasing the catalyst amount), the diameter of the NSBNSs decreases. The NSBNSs prepared at the $R_{B/C}$ of 1:0.5, 1:1 (Figure 2d,e), 1:2, and 1:4 are 4 μm, 3 μm, 1 μm, and 700 nm in diameter, respectively. Despite the difference in diameter, the spheres obtained at the above $R_{B/C}$ possess about a similar morphology, i.e., composed of radially oriented nanosheets. It can be seen that the sphere size can be controlled by changing the $R_{B/C}$.

Figure 4a shows a typical XRD pattern of the NSBNSs, where the peaks at 26.6, 42.0, 54.8, and 76.4° can be ascribed to the diffraction of (002), (100), (004), and (110) planes of hexagonal BN (JCPDS card No. 34-0421),[35] respectively. The sharpness of the main peaks and the appearance of the peaks related to the interplanar order such as (110) indicate that the NSBNSs are relatively well-crystallized. Figure 4b is a typical FTIR spectrum of the obtained NSBNSs. In the spectrum, two strong absorption peaks around 814 and 1396 cm^{-1} were observed, which are ascribed to the out-of-plane bending vibration of sp^2-bonded B-N-B and the in-plane stretching vibration of sp^2-bonded B-N, respectively. In addition, apart from the intrinsic peaks of hBN, several weak peaks were also observed. The peaks at 2875 and 2933 cm^{-1} are attributed to the B-NH_2 groups and that at 3450 cm^{-1} is attributed to the B-OH group.[32,33,36] As shown in Figure 4c, the Raman spectrum show a strong peak at about 1372 cm^{-1}, which is assigned to the BN E_{2g} mode. This Raman spectrum further confirms the well-crystallized hBN structure for the NSBNSs. The UV–visible absorption spectrum of the NSBNSs is shown in Figure 4d. In the spectrum, three absorption peaks are observed at about 213, 249, and 316 nm, respectively. The absorption peak at 213 nm (5.82 eV) corresponds to the band gap transition absorption of hBN.[37] The two small peaks at 249 nm (4.98 eV) and 316 nm (3.92 eV) are associated with defects such as vacancies and impurities.[38] The strong adsorption related to the band gap transition confirms the high crystallinity of the NSBNSs.

Figure 5 shows the TEM images of the NSBNSs prepared at the $R_{B/C}$ of 1:4 (panels a–c) and 1:1 (panels d–f). It is clearly revealed that the NSBNSs are composed of many ultrathin nanosheets, which are radially oriented with the sheet edges exposed on the surface. These nanosheets separate from each other, leading to much intersheet space. In agreement with the SEM observation, the size of the NSBNSs decreases with increasing the catalyst amount (Figure 5a,d). It is also noted that the nanosheet thickness decreases with increasing the catalyst amount, which was measured to be 3.1 and 9.1 nm for the $R_{B/C}$ of 1:4 and 1:1, respectively. On the high-resolution TEM images, straight and parallel lattice fringes can be observed (Figure 5b,c,e,f), suggesting high crystallinity of the NSBNSs. The average spacing between adjacent fringes is about 0.34 nm, corresponding to (002) crystal planes of hBN. For both samples, the nanosheets exhibit a tapered edge morphology and only several atomic layers remain at the edge positions (Figure 5c,f). The NSBNSs with the sheet edges oriented on the surface are attractive for adsorption application.

We found that the catalysts are indispensable for synthesizing the NSBNSs and no deposits can be obtained if only pure B powders were used. This is because the B source cannot be evaporated at the applied temperatures due to its high thermal stability. In order to understand the growth mechanism of the NSBNSs, the structural changes of the catalysts during the growth reaction was tested by XRD. Figure 6 shows the typical XRD patterns of the catalysts before and after reaction at 1300 °C. It was testified that the as-prepared catalyst is the mixture of $CoFe_2O_4$ and CoO. After growth reaction, the catalysts were converted into the mixture of FeB, FeB_{49}, CoB, FeCo, Fe_xN, $Co_2N_{0.67}$, and Co, where the metal borides predominate.

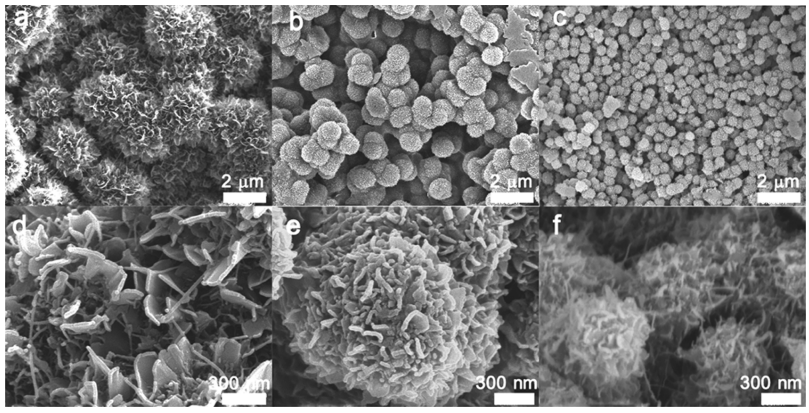

Figure 3. SEM images of the NSBNSs grown at different $R_{B/C}$: (a, d) 1:0.5, (b, e) 1:2, (c, f) 1:4.

DOI: 10.1021/am507491z
ACS Appl. Mater. Interfaces 2015, 7, 1824–1832

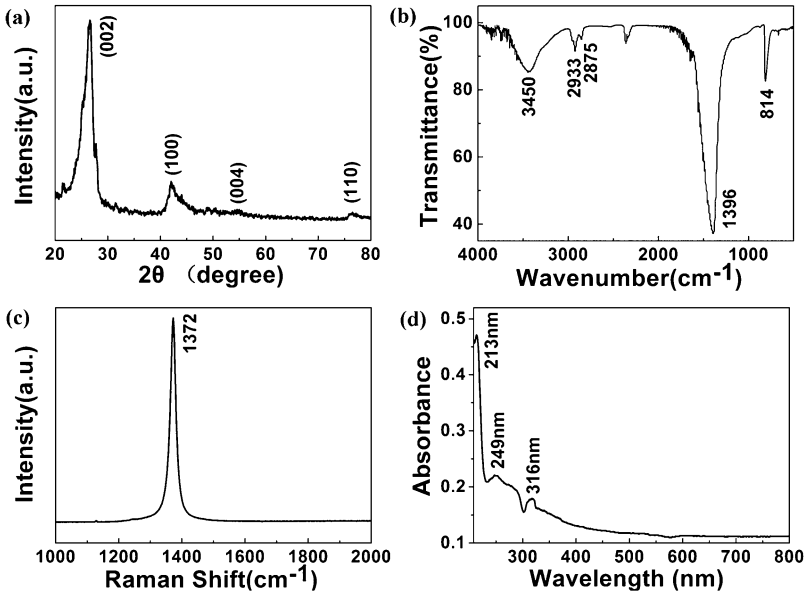

Figure 4. Typical XRD pattern (a), FTIR spectrum (b), Raman spectrum (c), and UV−visible absorption spectrum (d) of the NSBNSs.

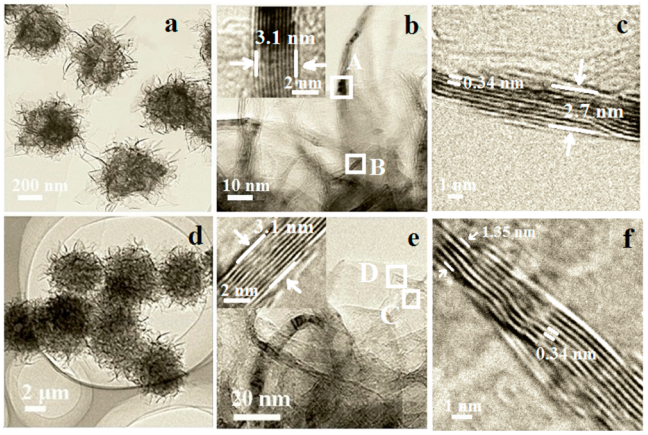

Figure 5. TEM images of the NSBNSs prepared at different $R_{B/C}$: (a−c) 1:4, (d−f) 1:1. (The insets of panels b and e are from the areas in rectangles A and C; panels c and f are from rectangles B and D, respectively.)

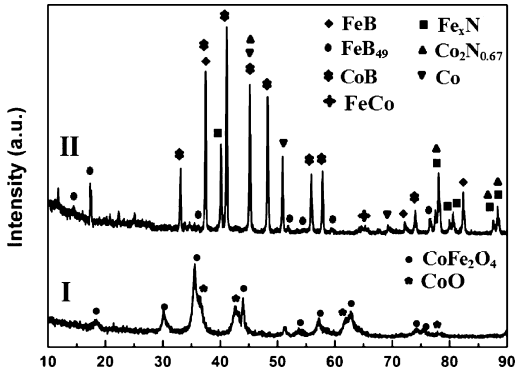

Figure 6. XRD patterns of the catalysts before (I) and after (II) the growth reaction.

Therefore, it is considered that the metal borides play key roles in the growth of the NSBNSs. At high temperature, $CoFe_2O_4$ and CoO react with B to form the metal borides, which possess higher reactivity than the pure B powders.[39] Therefore, the metal borides are capable of reacting with the active species generated by decomposition of NH_3, such as N, NH, NH_2, and H, at high temperature to form B containing volatile active species such as BN and BH_x, which deposit on the crucible walls to form the BN solid products. Concurrently, with the depletion of the B atoms in the metal borides, new B atoms are supplied from the B powders, making the metal borides exist stably. In this way, the B atoms can be evaporated continuously until they are exhausted. In our experiments, the amounts of the used B powders and catalysts are comparable; i.e., the B amount is limited relative to the catalyst. Therefore, the evaporating rate and the final amount of the evaporated B atoms decrease with decreasing the $R_{B/C}$, resulting in the corresponding decrease of the growth rate. As a result, the size and nanosheet thickness of the NSBNSs decrease with decreasing the $R_{B/C}$, as observed in the SEM and TEM images.

The N_2 adsorption/desorption isotherms of the different samples are shown in Figure 7. These isotherms exhibit a hysteresis loop in the P/P_0 range of 0.45−1.0, showing the features of type IV adsorption/desorption isotherms related to the mesoporous structure.[40] The specific surface area of the samples prepared at the $R_{B/C}$ of 1:0.5, 1:1, 1:2, and 1:4 were calculated to be 59.4, 92.7, 135.6, and 196.5 m^2/g, respectively.

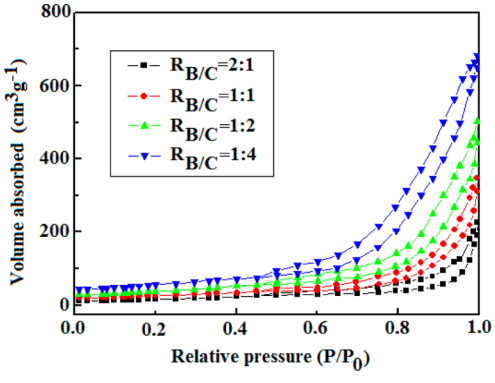

Figure 7. Nitrogen adsorption/desorption isotherms at 77 K of the samples prepared at 1300 °C and different $R_{B/C}$.

DOI: 10.1021/am507491z
ACS Appl. Mater. Interfaces 2015, 7, 1824−1832

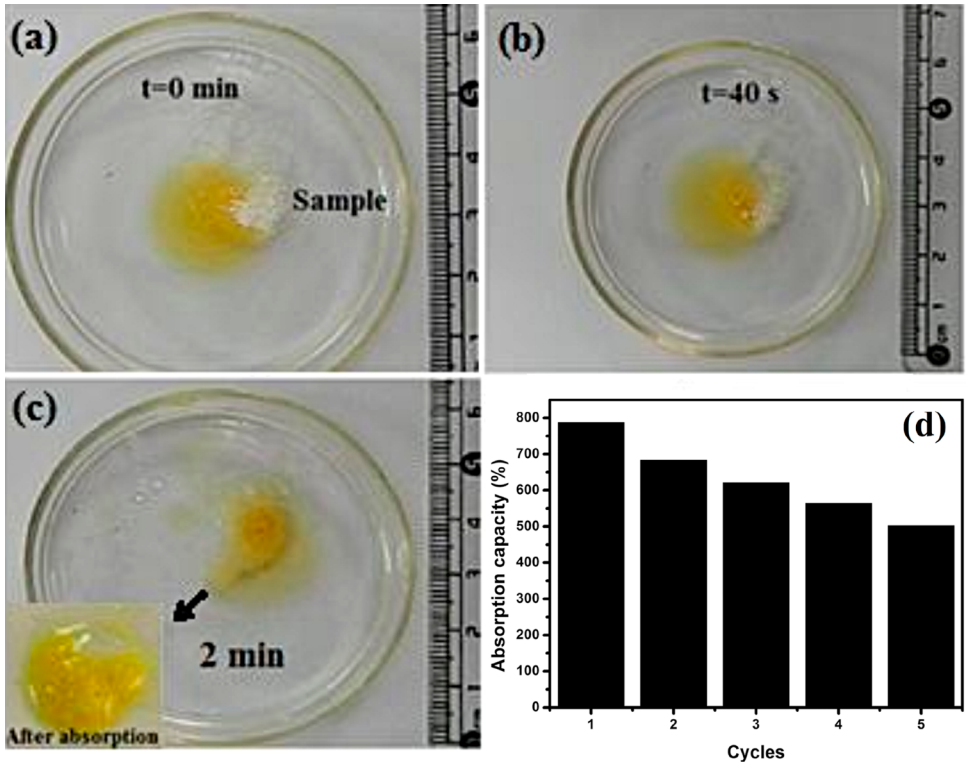

Figure 8. (a–c) Photographs showing the oil adsorption process of the NSBNSs (inset in (c) is the image of the oil-adsorbed NSBNSs taken out from the water after adsorption). (d) Reusability of NSBNSs regenerated by thermal treatment of adsorbed oil.

It is found that the SSA of the samples increases with decreasing the $R_{B/C}$ and the sample prepared at the $R_{B/C}$ of 1:4 possesses the highest SSA. The higher SSA for the samples prepared at a lower $R_{B/C}$ value results from the corresponding decrease of the sphere diameter and nanosheet thickness.

The above analyses indicate that the NSBNSs synthesized at $R_{B/C}$ = 1:4 possess the smallest diameter, smallest nanosheet thickness, and the highest SSA. Combining these characteristics and the high-density nanosheet edges on the surface and the dipolar nature of the B–N bonds, the NSBNSs ($R_{B/C}$ = 1:4) are highly advantageous for wastewater treatment. The oil adsorption capacity of the NSBNSs was evaluated by putting the sample into a mixture of water and oil, as shown in Figure 8a–c. When the NSBNSs contact the oil, the adsorbing process proceeded rapidly. Only after 40 s, a considerable part of the floating oil has been adsorbed. After 2 min, most of the oil has been taken up by the NSBNSs. After adsorption, the NSBNSs are still floating on the water surface and thus easily removed. The inset of Figure 8c is the image of the NSBNSs with the adsorbed oil taken out from the water. It is observed that the water became completely clear after adsorption. The adsorption capacity of the NSBNSs for oil was measured to be about 7.8 times their own weight, which is higher than the commercial bulk BN particles and activated carbon.[32] The reusability of the NSBNSs for oil absorption was investigated by heating the used NSBNSs at 600 °C in air for 2 h and then repeating the absorption process. After 5 recycles, the absorption capacity can still reach 540 wt % of its own weight, suggesting good recyclability (Figure 8d).

The adsorption performance of the NSBNSs on the dye pollutants was investigated using MG and MB as the paradigms. UV–visible adsorption spectra were measured at the maximum absorption wavelength of the dyes (MG and MB) to investigate their adsorption kinetics. Figure 9a,b shows the UV–visible adsorption spectra of the MG and MB solutions after adsorption for different times. It can be seen that the adsorption peak intensity decreased rapidly with increasing the adsorption time and became negligible within 60 min, indicating the high adsorbing efficiency of the NSBNSs on the dye molecules. We noted that the spectra of the 0 min absorption show an abnormal shape, which is caused by the too high absorption at the too high dye concentration. Figure 9c,d shows the relative concentration (C/C_0) of MG and MB versus adsorption time, indicating that about 99% of the dye molecules were removed within 180 min. Our experimental data fit the Langmuir adsorption isotherm quite well, with the correlation coefficients of 0.993 and 0.995 for MG and MB, respectively (Figure 9e,f). The maximum adsorption capacities of NSBNSs on MG and MB are 324 and 233 mg/g, respectively. It is noted that the adsorption capacity of the NSBNSs on MG is higher than those of adsorbents reported previously, such as PAA/SiO_2 composite nanofiber (220.49 mg/g),[41] treated ginger waste (84.03 mg/g),[42] and cyclodextrin-based adsorbent (91.9 mg/g).[43] The adsorption capacity of the NSBNSs on MB is comparable to or much higher than those of the reported adsorbents, such as the BN nanocarpets (272.4 mg/g),[31] activated carbon (15.59 mg/g),[44] coir pith carbon (5.87 mg/g),[45] and multiwalled carbon nanotubes (48.06 mg/g).[46]

The pollution of heavy metal ions has become a serious worldwide problem that endangers the environment and health of human beings. The typical heavy metal ions Cu^{2+}, Pb^{2+}, and Cd^{2+} were chosen to investigate the absorption performance of the NSBNSs. The initial concentrations of all the three metal ions were chosen at 200 mg/L, and the initial pH value is adjusted at 5.5. Figure 10a–c shows the relative concentration (C/C_0) of Cu^{2+}, Pb^{2+}, and Cd^{2+} versus adsorption time. It is

DOI: 10.1021/am507491z
ACS Appl. Mater. Interfaces 2015, 7, 1824–1832

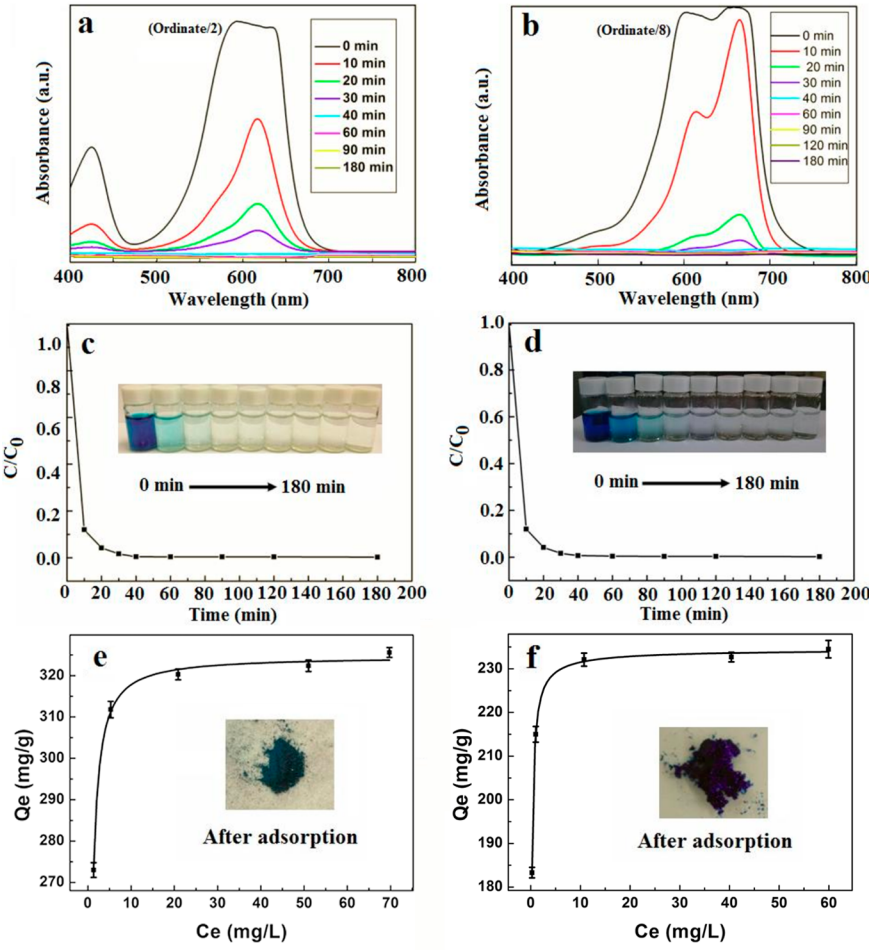

Figure 9. (a, b) UV−visible absorption spectra of the aqueous solutions of MG (110 mg/L, 25 mL) (a) and MB (110 mg/L, 25 mL) (b) at different adsorption times. (The insets show the respective molecular structure of MG and MB.) (c, d) Adsorption rates of MG (c) and MB (d) on NSBNSs. (The insets show the respective color of the MG and MB solutions at different adsorption times.) (e, f) Adsorption isotherms of MG (e) and MB (f) on NSBNSs. (The insets show the respective photographs of the NSBNSs after adsorption.)

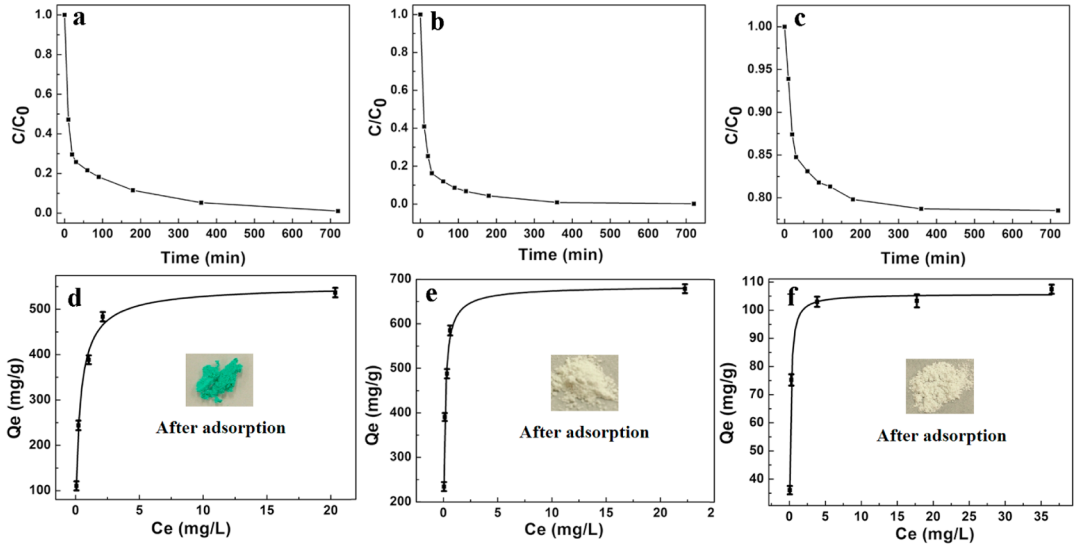

Figure 10. (a−c) Adsorption rates of the NSBNSs on Cu^{2+} (a), Pb^{2+} (b), and Cd^{2+} (c) in the solutions with an initial concentration of 200 mg/L and an initial pH value of 5.5. (d−f) Adsorption isotherms of the NSBNSs on Cu^{2+} (a), Pb^{2+} (b), and Cd^{2+} (c). (The insets show the respective photographs of the NSBNSs after adsorption.)

indicated that 99% of the Cu^{2+} and Pb^{2+} ions have been adsorbed after 720 min, manifesting an excellent property on Cu^{2+} and Pb^{2+} ions. However, the adsorption capacity of the NSBNSs on Cd^{2+} ions is relatively low and only 22% of the

DOI: 10.1021/am507491z
ACS Appl. Mater. Interfaces 2015, 7, 1824−1832

initial amount can be removed. The adsorption isotherms (Figure 10d–f) accord with the Langmuir model with the correlation coefficients at 0.986, 0.991, and 0.995 for the adsorption of Cu^{2+}, Pb^{2+}, and Cd^{2+}, respectively. The maximum adsorption capacities of Cu^{2+}, Pb^{2+}, and Cd^{2+} on NSBNSs are 536.7 ± 10.2, 678.7 ± 10.3, and 107.0 ± 1.4 mg/g, respectively. In previous reports, many materials, such as activated boron nitride, activated carbon, SWCNTs, oxidized CNTs, soy protein hollow microspheres (SPMs), hydroxyapatited nanosheet-assembled microspheres (HAP-NMSs), and graphene-oxide/ploy amidoamine dendrimers (GO/PAMAMs), have been used to adsorb Cu^{2+}, Pb^{2+}, and Cd^{2+} ions with different adsorption capacities. The activated boron nitride possesses an adsorption capacity of 225 mg/g on Pb^{2+} ion,[33] while the activated carbon possesses the adsorption capacities of 75.8 mg/g on Cu^{2+} and 94.4 mg/g on Pb^{2+}.[47] For the adsorbents of SWCNTs, oxidized CNTs, SPMs, HAP-NMSs, and GO/PAMAMs, the adsorption capacities on Cu^{2+}, Pb^{2+}, and Cd^{2+} ions range from 64.9 to 118.9 mg/g, 94.4 to 568.2 mg/g, and 55.8 to 253 mg/g,[48−52] respectively. Comparing with the above-reported adsorbents, the present NSBNSs show much higher adsorbing capacity on Cu^{2+} and Pb^{2+} ions, although their adsorption capacity on Cd^{2+} is not prominent. The changing trend of the adsorption capacity for the different ions is in accordance with the changing trend of their affinity, i.e., $Pb^{2+} > Cu^{2+} > Cd^{2+}$,[53] suggesting that the polarity of the B–N bonds may play roles in the adsorption of the metal ions.

The excellent adsorption performance of the NSBNSs arises from the intrinsic structure and properties of BN as well as the superior structure of the NSBNSs. The polarity of the B–N bonds provides high activity for adsorption, and the large interplane spacing provides the possibility for the molecules to intercalate.[33,54] It is noted that, in previous literatures, the high adsorption capacity was obtained mainly for the BN materials with very high SSA.[31−33] However, in the present work, the NSBNSs exhibit excellent adsorption performance despite the low SSA. It is considered that the excellent adsorption performance of the NSBNSs is caused by the radial orientation of the nanosheets, which makes the sheet edges crowd on the surface. These sheet edges possess high adsorption efficiency due to the high activity. In addition, the NSBNSs with the nanosheets radially aligned and separated from each other provide a smooth path for mass transport and enough space to accommodate the adsorbed pollutants. It is noted that the present method for preparing the NSBNSs could give a relatively high yield, and thus of high promise for practical application. Specifically, about 100 mg of the NSBNSs could be obtained in one single run in the small crucible (5 × 2.5 cm^2), suggesting the possibility of large-scale production.

4. CONCLUSIONS

In summary, we have successfully prepared the NSBNSs from B powders through a simple catalyzing thermal evaporation approach. The NSBNSs consist of radially oriented ultrathin nanosheets with the sheet edges oriented on the surface. The formation of the NSBNSs is strongly dependent on the reaction temperature and the mass ratio of the B source and the catalyst ($R_{B/C}$). By appropriately changing the temperature and $R_{B/C}$, the diameter and nanosheet thickness of the NSBNSs can be well-controlled. The NSBNSs possess excellent performance for application as adsorbents removing oil, dyes, and heavy metal ions from water. The oil uptake reaches 7.8 times its own weight. The adsorption capacities for malachite green and methylene blue are 324 and 233 mg/g, while those for Cu^{2+}, Pb^{2+}, and Cd^{2+} are 678.7, 536.7, and 107.0 mg/g, respectively. In particular, the adsorption capacities for Pb^{2+} and Cu^{2+} are higher or much higher than those of the adsorbents reported previously. The excellent adsorption performance of the NSBNSs mainly originates from the high-density edge sites on the surface. These results suggest that the present NSBNSs are promising for water treatment and cleaning.

AUTHOR INFORMATION

Corresponding Author

*E-mail: jyu@hitsz.edu.cn. Fax: +86-755-26033504. Tel: +86-755-26033478 (J.Y.).

Notes

The authors declare no competing financial interest.

ACKNOWLEDGMENTS

This work is supported by the National Basic Research Program of China (2012CB933003), the National Natural Science Foundation of China (no. 51272057), and the Shenzhen Basic Research Program (JCYJ20130329150737027).

REFERENCES

(1) Stankovich, S.; Dikin, D. A.; Piner, R. D.; Kohlhaas, K. A.; Kleinhammes, A.; Jia, Y. Y.; Wu, Y.; Nguyen, S. T.; Ruoff, R. S. Synthesis of Grapheme-Based Nanosheets via Chemical Reduction of Exfoliated Graphite Oxide. *Carbon* **2007**, *45*, 1558–1565.

(2) Wang, J. J.; Zhu, M. Y.; Outlaw, R. A.; Zhao, X.; Manos, D. M.; Holloway, B. C. Synthesis of Carbon Nanosheets by Inductively Coupled Radio-Frequency Plasma Enhanced Chemical Vapor Deposition. *Carbon* **2004**, *42*, 2867–2872.

(3) Wen, Q.; Wang, S. Y.; Yan, J.; Cong, L. J.; Chen, Y.; Xi, H. Y. Porous Nitrogen-Doped Carbon Nanosheet on Graphene as Metal-Free Catalyst for Oxygen Reduction Reaction in Air-Cathode Microbial Fuel Cells. *Bioelectrochemistry* **2014**, *95*, 23–28.

(4) Shang, N. G.; Papakonstantinou, P.; McMullan, M.; Chu, M.; Stamboulis, A.; Potenza, A.; Dhesi, S. S.; Marchetto, H. Catalyst-Free Efficient Growth, Orientation and Biosensing Properties of Multilayer Graphene Nanoflake Films with Sharp Edge Planes. *Adv. Funct. Mater.* **2008**, *18*, 3506–3514.

(5) Zhao, L.; Qiu, Y. J.; Yu, J.; Deng, X. Y.; Dai, C. L.; Bai, X. D. Carbon Nanofibers with Radially Grown Graphene Sheet Derived from Electrospinning for Aqueous Supercapacitors with High Working Voltage and Energy Density. *Nanoscale* **2013**, *5*, 4902–4909.

(6) Zhao, L.; Yu, J.; Li, W. J.; Wang, S. G.; Dai, C. L.; Wu, J. W.; Bai, X. D.; Zhi, C. Y. Honeycomb Porous MnO_2 Nanofibers Assembled from Radially Grown Nanosheets for Aqueous Supercapacitors with High Working Volage and Energy Density. *Nano Energy* **2014**, *4*, 39–48.

(7) Shang, N. G.; Au, F. C. K.; Meng, X. M.; Lee, C. S.; Bello, I.; Lee, S. T. Uniform Carbon Nanoflake Films and Their Field Emissions. *Chem. Phys. Lett.* **2002**, *358*, 187–191.

(8) Yoo, E. J.; Kim, J.; Hosono, E.; Zhou, H. S.; Kudo, T.; Honma, I. Large Reversible Li Storage of Graphene Nanosheet Families for Use in Rechargeable Lithium Ion Batteries. *Nano Lett.* **2008**, *8*, 2277–2282.

(9) Wang, B.; Park, J.; Wang, C. Y.; Ahn, H.; Wang, G. X. Mn_3O_4 Nanoparticles Embedded into Grapheme Nanosheets: Preparation, Characterization, and Electrochemical Properties for Supercapacitors. *Electrochim. Acta* **2010**, *55*, 6812–6817.

(10) Wu, Y. H.; Qiao, P. W.; Chong, T. C.; Shen, Z. X. Carbon Nanowalls Grown by Microwave Plasma Enhanced Chemical Vapor Deposition. *Adv. Mater.* **2002**, *14*, 64–67.

DOI: 10.1021/am507491z
ACS Appl. Mater. Interfaces 2015, 7, 1824–1832

(11) Zhu, L. P.; Liao, G. H.; Bing, N. C.; Wang, L. L.; Yang, Y.; Xie, H. Y. Self-Assembled 3D BiOCl Hierarchitectures: Tunable Synthesis and Characterization. *CrystEngComm* **2010**, *12*, 3791−3796.
(12) Wu, Z. S.; Yang, S. B.; Sun, Y.; Parvez, K.; Feng, X. L.; Müllen, K. 3D Nitrogen-Doped Graphene Aerogel-Supported Fe_3O_4, Nanoparticles as Efficient Electrocatalysts for the Oxygen Reduction Reaction. *J. Am. Chem. Soc.* **2012**, *134*, 9082−9085.
(13) Ye, S. B.; Feng, J. C.; Wu, P. Y. Deposition of Three-Dimensional Graphene Aerogel on Nickel Foam as a Binder-Free Supercapacitor Electrode. *ACS Appl. Mater. Interfaces* **2013**, *5*, 7122−7129.
(14) Zhi, C. Y.; Bando, Y.; Tang, C. C.; Xie, R. G.; Sekiguchi, T.; Golberg, D. Perfectly Dissolved Boron Nitride Nanotubes due to Polymer Wrapping. *J. Am. Chem. Soc.* **2005**, *127*, 15996−15997.
(15) Liu, F.; Yu, J.; Bai, X. D. Crystallinity Improvement of Hexagonal Boron Nitride Films by Molybdenum Catalysts during Microwave Plasma Chemical Vapor Deposition and Post-Annealing. *Appl. Surf. Sci.* **2012**, *258*, 10191−10194.
(16) Yang, X. X.; Guan, Z. X.; Zeng, M.; Wei, J. K.; Wang, W. L.; Bai, X. D. Facile Synthesis of Large-Area Ultrathin Hexagonal BN Films via Self-Limiting Growth at the Molten B_2O_3 Surface. *Small* **2013**, *9*, 1353−1358.
(17) Zhi, C. Y.; Hanagata, N.; Bando, Y.; Golberg, D. Dispersible Shortened Boron Nitride Nanotubes with Improved Molecule-Loading Capacity. *Chem.—Asian J.* **2011**, *6*, 2530−2535.
(18) Sajjad, M.; Morell, G.; Feng, P. Advance in Novel Boron Nitride Nanosheets to Nanoelectronic Device Applications. *ACS Appl. Mater. Interfaces* **2013**, *5*, 5051−5056.
(19) Kubota, Y.; Watanabe, K.; Tsuda, O.; Taniguchi, T. Deep Ultraviolet Light- Emitting Hexagonal Boron Nitride Synthesized at Atmospheric Pressure. *Science* **2007**, *317*, 932−934.
(20) Zhang, Y. M.; He, X. D.; Han, J. C.; Du, S. Y. Combustion Synthesis of Hexagonal Boron-Nitride Based Ceramics. *J. Mater. Process. Technol.* **2001**, *116*, 161−164.
(21) Zhou, S. J.; Ma, C. Y.; Meng, Y. Y.; Su, H. F.; Zhu, Z.; Deng, S. L.; Xie, S. Y. Activation of Boron Nitride Nanotubes and Their Polymer Composites for Improving Mechanical Performance. *Nanotechnology* **2012**, *23*, 055708.
(22) Yu, J.; Qin, L.; Hao, Y. F.; Kuang, S. S.; Bai, X. D.; Chong, Y. M.; Zhang, W. J.; Wang, E. G. Vertically Aligned Boron Nitride Nanosheets: Chemical Vapor Synthesis, Ultraviolet Light Emission, and Superhydrophobicity. *ACS Nano* **2010**, *4*, 414−422.
(23) Postole, G.; Gervasini, A.; Guimon, C.; Auroux, A.; Bonnetot, B. Influence of the Preparation Method on the Surface Characteristics and Activity of Boron-Nitride-Supported Noble Metal Catalysts. *J. Phys. Chem. B* **2006**, *110*, 12572−12580.
(24) Weng, Q. H.; Wang, X. B.; Zhi, C. Y.; Bando, Y.; Golberg, D. Boron Nitride Porous Microbelts for Hydrogen Storage. *ACS Nano* **2013**, *7*, 1558−1565.
(25) Lee, C. H.; Wang, J. S.; Kayatsha, V. K.; Huang, J. Y.; Yap, Y. K. Effective Growth of Boron Nitride Nanotubes by Thermal Chemical Vapor Deposition. *Nanotechnology* **2008**, *19*, 455605.
(26) Chen, Z. G.; Zou, J.; Liu, G.; Li, F.; Wang, Y.; Wang, L. Z.; Yuan, X. L.; Sekiguchi, T.; Cheng, H. M.; Lu, G. Q. Novel Boron Nitride Hollow Nanoribbons. *ACS Nano* **2008**, *2*, 2183−2191.
(27) Qiu, Y. J.; Yu, J.; Rafique, J.; Yin, J.; Bai, X. D.; Wang, E. G. Large-Scale Production of Aligned Long Boron Nitride Nanofibers by Multijet/ Multicollector Electrospinning. *J. Phys. Chem. C* **2009**, *113*, 11228−11234.
(28) Shen, J. M.; Feng, Y. T. Formation of Flower-Like Carbon Nanosheet Aggregations and Their Electrochemical Application. *J. Phys. Chem. C* **2008**, *112*, 13114−13120.
(29) Zhang, W.; Zhou, W. D.; Wright, J. H.; Kim, Y. N.; Liu, D. W.; Xiao, X. C. Mn-Doped TiO_2 Nanosheet-Based Spheres as Anode Materials for Lithium-Ion Batteries with High Performance at Elevated Temperatures. *ACS Appl. Mater. Interfaces* **2014**, *6*, 7292−7300.
(30) Wu, H. B.; Chen, J. S.; Lou, X. W.; Hng, H. H. Synthesis of SnO_2 Hierarchical Structures Assembled from Nanosheets and Their Lithium Storage Properties. *J. Phys. Chem. C* **2011**, *115*, 24605−24610.
(31) Zhang, X.; Lian, G.; Zhang, S. J.; Cui, D. L.; Wang, Q. L. Boron Nitride Nanocarpets: Controllable Synthesis and Their Adsorption Performance to Organic Pollutants. *CrystEngComm* **2012**, *14*, 4670−4676.
(32) Lei, W. W.; Portehault, D.; Liu, D.; Qin, S.; Chen, Y. Porous Boron Nitride Nanosheets for Effective Water Cleaning. *Nat. Commun.* **2013**, *4*, 1777.
(33) Li, J.; Xiao, X.; Xu, X. W.; Lin, J.; Huang, Y.; Xue, Y. M.; Jin, P.; Zou, J.; Tang, C. C. Activated Boron Nitride as an Effective Adsorbent for Metal Ions and Organic Pollutants. *Sci. Rep.* **2013**, *3*, 3208.
(34) Bertran, C. A.; Silva, N. T. D.; Thim, G. P. Citric Acid Effect on Aqueous Sol-Gel Cordierite Synthesis. *J. Non-Cryst. Solids* **2000**, *273*, 140−144.
(35) Paine, R. T.; Narula, C. K. Synthetic Routes to Boron Nitride. *Chem. Rev.* **1990**, *90*, 73−91.
(36) Huang, C. J.; Chen, C.; Ye, X. X.; Ye, W. Q.; Hu, J. L.; Xu, C.; Qiu, X. Q. Stable Colloidal Boron Nitride Nanosheet Dispersion and Its Potential Application in Catalysis. *J. Mater. Chem. A* **2013**, *1*, 12192−12197.
(37) Pakdel, A.; Wang, X. B.; Zhi, C. Y.; Bando, Y.; Watanabe, K.; Sekiguchi, T.; Nakayama, T.; Golberg, D. Facile Synthesis of Vertically Aligned Hexagonal Boron Nitride Nanosheets Hybridized with Graphitic Domains. *J. Mater. Chem.* **2012**, *22*, 4818−4824.
(38) Zhao, Z. Y.; Yang, Z. G.; Wen, Y.; Wang, Y. H. Facile Synthesis and Characterization of Hexagonal Boron Nitride Nanoplates by Two-Step Route. *J. Am. Ceram. Soc.* **2011**, *94*, 4496−4501.
(39) Zhang, L. P.; Zhang, G.; Chen, C. S.; Li, L.; Xia, T. L.; Shi, K. Y. A Facile Route to Synthesise h-BN-FeB_{49} Nanocomposites with Magnetic and Fluorescent Properties. *CrystEngComm* **2011**, *13*, 7153−7160.
(40) Kruk, M.; Jaroniec, M. Gas Adsorption Characterization of Ordered Organic-Inorganic Nanocomposite Materials. *Chem. Mater.* **2001**, *13*, 3169−3183.
(41) Xu, R.; Jia, M.; Zhang, Y. L.; Li, F. T. Sorption of Malachite Green on Vinyl-Modified Mesoporous Poly(acrylic acid)/SiO_2 Composite Nanofiber Membranes. *Microporous Mesoporous Mater.* **2012**, *149*, 111−118.
(42) Ahmad, R.; Kumar, R. Adsorption Studies of Hazardous Malachite Green onto Treated Ginger Waste. *J. Environ. Manage.* **2010**, *91*, 1032−1038.
(43) Crini, G.; Peindy, H. N.; Gimbert, F.; Robert, C. Removal of C.I. Basic Green 4 (Malachite Green) from Aqueous Solutions by Adsorption Using Cyclodextrin-Based Adsorbent: Kinetic and Equilibrium Studies. *Sep. Purif. Technol.* **2007**, *53*, 97−110.
(44) Sharma, Y. C.; Uma; Sinha, A. S. K.; Upadhyay, S. N. Characterization and Adsorption Studies of *Cocos nucifera L.* Activated Carbon for the Removal of Methylene Blue from Aqueous Solutions. *J. Chem. Eng. Data* **2010**, *55*, 2662−2667.
(45) Kavitha, D.; Namasivayam, C. Experimental and Kinetic Studies on Methylene Blue Adsorption by Coir Pith Carbon. *Bioresour. Technol.* **2007**, *98*, 14−21.
(46) Ai, L. H.; Zhang, C. Y.; Liao, F.; Wang, Y.; Li, M.; Meng, L. Y.; Jiang, J. Removal of Methylene Blue from Aqueous Solution with Magnetite Loaded Multi-Wall Carbon Nanotube: Kinetic, Isotherm and Mechanism Analysis. *J. Hazard. Mater.* **2011**, *198*, 282−290.
(47) Anirudhan, T. S.; Sreekumari, S. S. Adsorptive Removal of Heavy Metal Ions from Industrial Effluents Using Activated Carbon Derived from Waste Coconut Buttons. *J. Environ. Sci.* **2011**, *23*, 1989−1998.
(48) Moradi, O.; Zara, K.; Yari, M. Interaction of Some Heavy Metal Ions with Single Walled Carbon Nanotube. *Int. J. Nano Dimens.* **2011**, *1*, 203−220.
(49) Tofighy, M. A.; Mohammadi, T. Adsorption of Divalent Heavy Metal Ions from Water using Carbon Nanotube Sheets. *J. Hazard. Mater.* **2011**, *185*, 140−147.
(50) Liu, D. G.; Li, Z. H.; Li, W.; Zhong, Z. R.; Xu, J. Q.; Ren, J. J.; Ma, Z. S. Adsorption Behavior of Heavy Metal Ions from Aqueous Solution by Soy Protein Hollow Microspheres. *Ind. Eng. Res.* **2013**, *52*, 11036−11044.

DOI: 10.1021/am507491z
ACS Appl. Mater. Interfaces 2015, 7, 1824−1832

(51) Zhao, X. Y.; Zhu, Y. J.; Zhao, J.; Lu, B. Q.; Chen, F.; Qi, C.; Wu, J. Hydroxyapatite Nanosheet-Assembled Microspheres: Hemoglobin-Templated Synthesis and Adsorption for Heavy Metal Ions. *J. Colloid Interface Sci.* **2014**, *416*, 11−18.
(52) Zhang, F.; Wang, B.; He, S. F.; Man, R. L. Preparation of Graphene-Oxide/Polyamidoamine Dendrimers and Their Adsorption Properties toward Some Heavy Metal Ions. *J. Chem. Eng. Data* **2014**, *59*, 1719−1726.
(53) Lv, L.; Hor, M. P.; Su, F. B.; Zhao, X. S. Competitive Adsorption of Pb^{2+}, Cu^{2+}, and Cd^{2+} Ions on Microporous Titanosilicate ETS-10. *J. Colloid Interface Sci.* **2005**, *287*, 178−184.
(54) Lian, G.; Zhang, X.; Zhang, S. J.; Liu, D.; Cui, D. L.; Wang, Q. L. Controlled Fabrication of Ultrathin-Shell BN Hollow Spheres with Excellent Performance in Hydrogen Storage and Wastewater Treatment. *Energy Environ. Sci.* **2012**, *5*, 7072−7080.

DOI: 10.1021/am507491z
ACS Appl. Mater. Interfaces 2015, 7, 1824−1832